Citation info:
Cavaliere, Davide and Fezans, Nicolas and Kiehn, Daniel and Quero-Martin, David and Vrancken, Patrick (2022) Gust Load Control Design Challenge Including Lidar Wind Measurements and Based on the Common Research Model. In: AIAA SciTech 2022 Forum. AIAA SciTech 2022, San Diego, California, USA. doi: 10.2514/6.2022-1934, ISBN 978-162410631-6.

Gust Load Control Design Challenge Including Lidar Wind Measurements and Based on the Common Research Model

Davide Cavaliere*, Nicolas Fezans†, and Daniel Kiehn‡
DLR (German Aerospace Center), Braunschweig, Germany

David Quero Martin§
DLR (German Aerospace Center), Göttingen, Germany

Patrick Vrancken¶
DLR (German Aerospace Center), Oberpfaffenhofen, Germany

Active load alleviation systems are key to enabling the design of lighter structures by reducing structural loads. The ongoing development of gust detection systems based on a Doppler lidar sensor has created the opportunity to design powerful gust load alleviation controllers with access to the wind field over 100 m ahead of the aircraft. The present paper describes a highly representative public benchmark for lidar-based gust load alleviation. It is based on a linear aeroservoelastic model of the Common Research Model (CRM), a surrogate model of a Doppler wind lidar sensor, and a wind reconstruction algorithm. An active gust load alleviation control design challenge based on this benchmark is proposed, and an example of a lidar-based controller is designed and evaluated against this challenge.

I. Nomenclature

A_{Rx}	=	Lidar receiver telescope size
C_D	=	Aerodynamic drag coefficient
C_L	=	Aerodynamic lift coefficient
EAS	=	Equivalent Air Speed
e	=	Electron charge
E_p	=	Laser pulse energy
g	=	Gravitational acceleration at the Earth's surface (9.81 m/s^2)
h	=	Altitude
HTP	=	Horizontal tail plane
Lidar	=	Light Detection and Ranging (also LIDAR or LiDAR)
m	=	Aircraft mass
N_e	=	Number of photo-electrons corresponding to a lidar measurement
PAP	=	Power aperture product
PRF	=	Pulse Repetition Frequency
P_{Tx}, P_{Tx}	=	Transmitted and received optical power, respectively
R	=	Measurement range
ΔR	=	Range gate (spatial resolution)
r_{refresh}	=	Measurement refresh rate
s	=	Laplace transform complex frequency variable
S	=	Reference lifting surface area

*PhD Student, DLR, Institute of Flight Systems, Lilienthalplatz 7, 38108 Braunschweig, Germany, AIAA Member. E-mail: davide.cavaliere@dlr.de
†Scientific Advisor, DLR, Institute of Flight Systems, Lilienthalplatz 7, 38108 Braunschweig, Germany, AIAA Senior Member. E-mail: nicolas.fezans@dlr.de
‡Research Scientist, DLR, Institute of Flight Systems, Lilienthalplatz 7, 38108 Braunschweig, Germany. E-mail: daniel.kiehn@dlr.de
§Research Scientist, DLR, Institute of Aeroelasticity, Bunsenstr. 10, 37073 Göttingen, Germany. E-mail: david.queromartin@dlr.de
¶Research Scientist, DLR, Institute of Atmospheric Physics, Münchener Str. 20, 82234 Weßling, Germany. E-mail: patrick.vrancken@dlr.de

SNR	=	Signal-to-noise ratio
T	=	Static temperature
T_{atm}	=	Atmospheric transmissivity
TAS	=	True Air Speed
α	=	Angle of attack
β_{mol}	=	Molecular backscatter coefficient
γ	=	Flight path angle
η_{opt}	=	Overall optical efficiency of receiver and transmitter setup
$\kappa_{v_{real}}$	=	Correction factor to consider that the amount of spectral channels is finite
κ_{TIF}	=	Correction factor for the uncertainty of the implementation (technology implementation factor)
λ	=	Laser wavelength
$\sigma_{v,ss}, \sigma_{v,av}$	=	Standard deviation of a LOS wind measurement for a single 'shot' and with averaging, respectively
ρ	=	Air density
ρ_{det}	=	Detector responsitivity
θ	=	Parameter vector being optimized in the maximum-likelihood wind reconstruction
Θ	=	Pitch attitude
$\tau_{\text{lead}}, \tau_{\text{lag}}$	=	Lead and lag times defining the boundaries of the wind reconstruction mesh

II. Introduction

The development of lighter, more efficient aircraft is a key element in continuing efforts to create a sustainable aviation industry. One approach to this problem is implementing active load alleviation systems to reduce structural loads, thereby enabling the design of lighter and more flexible structures. Although wing loads are often strongly dependent on limit maneuver requirements, gust and turbulence certification requirements can also produce sizing loads, especially for large, flexible aircraft.

The design of active gust load alleviation systems is characterized by the dynamic and unpredictable nature of atmospheric turbulence. Feedback control can be used to improve structural dynamics, for instance by effectively increasing modal damping. Historically, most industrial examples of gust load alleviation systems, such as the C-5A ALDCS, the L-1011-500 ACS, or the A320 LAF, were based on feedback controllers using local inertial sensors to detect structural accelerations [1].

These types of systems are successful at reducing fatigue loads, however their ability to achieve significant reductions in peak loads is limited by system delays and dynamics. Feedforward control, combined with sufficiently early gust detection, can instead compensate for system limitations to coordinate control actions with the gust's impact on the airframe. Effective feedforward gust load alleviation thus depends on the gust detection system: the achievable performance is limited by both the lead time and the precision of the gust information.

Past designs have relied on angle-of-attack sensors placed near the nose and a direct-lift-control strategy, such as in the DLR LARS project, [2]. More recently, lidar sensors capable of detecting atmospheric disturbances ahead of the aircraft have been the subject of research. One such lidar system was designed and tested in flight as part of the AWIATOR project [3], and the technology has been further developed since then [4, 5]. The large lead time afforded by a lidar system, potentially over 100 m ahead of the aircraft, not only compensates for system delays, but also enables the use of a pitching strategy to take advantage of the short period mode's load-alleviation potential.

Such a lidar-based system (including sensor itself and post-processing algorithms) is fairly complex and, to the best of the authors' knowledge, no such model is freely available. Various researchers (see for instance [6, 7]) have also been looking at the way wind information ahead of the aircraft can be used for active load alleviation with various assumptions regarding the properties (e.g. quality, noise) of the wind information. With the aim of fostering cooperation and exchanges in the community, a benchmark model has been created and is hereby shared. It consists of the sensor simulation and the wind reconstruction algorithm from [4], an aeroservoelastic model based on the Common Research Model (CRM), a basic controller (serving as example), and various scripts permitting to evaluate the results based on a hybrid simulation environment (mixing discrete-time controllers and the continuous-time aeroservoelastic aircraft model).

The benchmark introduced hereafter constitutes a highly representative test case for a large flexible long-range airplane configuration. It features a lidar sensor system but can also be used for gust load alleviation research with more classical sensors: users can simply ignore the wind measurements from the lidar in their controller. It can be downloaded freely on `https://github.com/dlr-ft-gla/GLA-Benchmark` . The authors of the present paper

intend to maintain a list of published papers using this benchmark and kindly ask users who have work with it and published papers using it to send us the corresponding references. Researchers can also share their controllers or any new feature added to the benchmark with the community; for this, the easiest way is to fork the benchmark repository, to commit the new features, controllers, etc. in the forked repository and to send a pull request.

The aircraft aeroservoelastic model is described in section III. Section IV presents the way the gusts are modeled, sensed with the lidar sensor, and reconstructed. Section V introduces the concept of lidar-based gust alleviation control, section VI describes the hybrid simulation architecture, and section VII defines a benchmark gust load alleviation control design problem. Finally, section VIII describes the design of the benchmark's default controller and its evaluation against the benchmark problem.

III. Aircraft Model

A. Common Research Model

The external geometry of the Common Research Model (CRM) was originally developed by NASA and Boeing as a benchmark for CFD studies, and was released for the 4th Drag Prediction Workshop [8].* It was designed to be representative of a conventional widebody commercial transport aircraft optimized for transonic flight. The CRM-FERMAT model is a further development of the CRM for aeroelastic studies [9] which introduced a structural model, a vertical tailplane, engine nacelles, and control surfaces, as well as the possibility to define multiple mass configurations.

Broadly speaking, the aircraft is similar in size and configuration to a Boeing 777. Its basic characteristics are described in Table 1. The flight point used in this benchmark corresponds to mass case C2 (MTOW, 100 % fuel), center of gravity (CG) at 25 % MAC (i.e. 31.4 m from the nose), and 9100 m altitude.

Table 1 Characteristics of the CRM-FERMAT model.

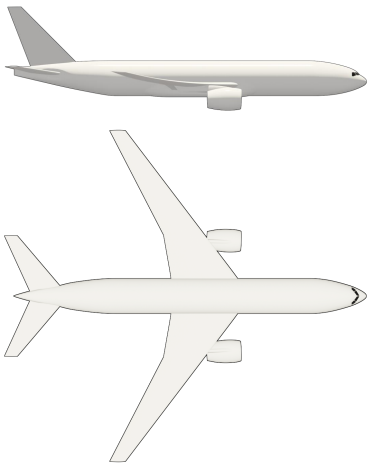

CRM-FERMAT Characteristics

Aircraft parameter	Value
Fuselage length	62.75 m
Fuselage diameter	6.2 m
Wingspan	58 m
Reference chord	7.005 m
Wing area	383.7 m^2
Leading edge wing sweep	35°
Maximum Takeoff Weight (MTOW)	260,000 kg
Maximum Zero Fuel Weight (MZFW)	195,000 kg
Operating Empty Weight (OEW)	134,000 kg
Center of Gravity range (% MAC)	14 % - 40 %

*https://commonresearchmodel.larc.nasa.gov/

B. CRM-FERMAT Aeroelastic Model

In this section, the tangential interpolation method as described in [10] based on the Loewner framework is applied. This is applied to the unsteady aerodynamic model described by the doublet lattice method (DLM) appropriate for subsonic compressible flow (neglecting nonlinear compressible and inviscid terms) containing a total of 1910 panels for this configuration, and is afterwards coupled with the structural model in order to obtain the complete aeroelastic model. Later on, the required actuator and sensor elements are added, as explained in next sections.

The input of the aerodynamic system is defined by the vertical atmospheric disturbance at a particular spatial location (the aircraft nose) and a set of generalized coordinates corresponding to the control surfaces and the structural modes, together with their first and second time derivatives. The aerodynamic forces due to the structural deformation and the control surface deflections are evaluated by means of a transpiration boundary condition by applying a variation of downwash velocity on the related aerodynamic panels while keeping the original panel geometry.

The generation of the aeroelastic state-space model is now briefly described. For details the reader is referred to [10]. Setting the Mach number to $M_\infty = 0.86$, the reference length for the reduced frequency to $L_{ref} = 7$ m, and collecting the frequency-domain data from the DLM solver, a Loewner realization is first obtained. Next, in order to convert the obtained generalized state-space form corresponding to a descriptor realization into a standard set of ordinary differential equations (ODEs) represented by a state-space model, a residualization together with a stabilization procedure are imposed. In this work, this is done by carrying out a vector fit with a rational and a second-order polynomial part. Note that the poles are already known from the Loewner realization. In case there are some unstable poles, they are mirrored with respect to the imaginary axis prior to the fitting. Upon completing the fit, a Gilbert realization allows the rational part to be obtained in the form of standard state-space matrices. The polynomial part is responsible for the dependence on the first and second time derivatives of the generalized coordinates and the control surfaces.

Once the aerodynamic system has been obtained in a standard state-space form, it is analytically coupled with the structural dynamics equations. These are defined by the corresponding generalized mass and stiffness matrices, whereas the structural damping has been neglected. A total of 16 symmetric flexible modes ranging in frequencies from 1.05 Hz up to 16.37 Hz together with heave and pitch rigid-body modes have been considered. A total of 6 control surfaces (two inner ailerons, two outer ailerons and two elevators) have been included. In order to transfer the forces and displacements between the structural and aerodynamic domains, the thin plate spline (TPS) has been used.

The resulting aeroelastic model in state-space form has as inputs the vertical wind speed at the aircraft nose and the control surface deflections, rates, and accelerations (which are afterwards suppressed from the standard state-space form through the use of transfer functions for the control surface actuators of second or higher order, see III.D). For more details see [10]. A final reduction based on balanced truncation has been applied, resulting in a total number of 232 states for the aeroelastic model without including the sensors and actuators. The structural loads are retrieved by applying the force summation method (FSM) so as to minimize the influence of the number of retained structural modes on the load values, and correspondingly included in the output of the state-space model. Additional quantities for monitoring and evaluation are included in the output vector as well, including the rigid-body motion and the generalized coordinates.

C. Phugoid Augmentation

The inclusion of vertical speed in the aeroelastic model without the corresponding variations in airspeed results in a partially-modeled phugoid mode. This partial phugoid manifests itself as a very slow unstable real pole, which is in turn problematic for control design. As mentioned in [2], longitudinal acceleration caused by gust alleviation can play an important role in determining the aircraft's ride quality. The drawbacks in terms of passenger comfort of using direct-lift control (DLC) flaps for load alleviation were observed at the time using the DLR ATTAS aircraft: the vertical accelerations were significantly reduced but at the expense of increased longitudinal accelerations due to the variations in aerodynamic drag.

The benchmark model provided was partly derived from potential aerodynamic methods, which do not predict drag properly for such use. The CRM-FERMAT aeroelastic model (cf. section III.B) also does not contain the necessary states for including the phugoid mode and speed variations. This model is therefore augmented with an approximate phugoid mode to make it more representative at very low frequencies, which might play a role for a baseline "rigid-body" control function. The model's primary intended use is the investigation of active gust load alleviation functions which can usually be made with models that do not include phugoid motion. Nevertheless, including the following approximation is quite easy and it is expected to provide a more representative simulation when not only considering the gust load alleviation function but also some "rigid-body" control function as well.

$$\dot{E}_{tot} = \dot{E}_k + \dot{E}_p = mV\dot{V} + mg\dot{h} = P_{ext} = -P_D + P_T + P_{gust} \tag{1}$$

The approach for the phugoid augmentation is based on the total energy equilibrium shown in Eq. 1. Total energy E_{tot} is given by the sum of kinetic energy $E_k = \frac{1}{2}mV^2$ and potential energy $E_p = mgh$. The variation in total energy is caused by external forces, whose power P_{ext} includes drag (P_D), thrust (P_T), and atmospheric turbulence (P_{gust}). The following assumptions and simplifications are then made:

- The aircraft is in trimmed level flight in calm air, resulting in Eq. 2.

$$\dot{E}_{tot,0} = \dot{E}_{k,0} = \dot{E}_{p,0} = \dot{h}_0 = \dot{V}_0 = P_{gust,0} = P_{T,0} - P_{D,0} = 0 \tag{2}$$

  In Eq.2, the subscript 0 refers to the equilibrium state, e.g. V_0 is the trimmed true airspeed (TAS).
- Variations in the drag coefficient include only induced drag caused by variations in lift, as in Eq. 3.

$$\delta C_D = \frac{\partial C_D}{\partial C_L}\delta C_L = \frac{\partial C_D}{\partial C_L}\frac{\partial C_L}{\partial \alpha}\delta\alpha \tag{3}$$

- Aerodynamic angle of attack is approximated by the inertial angle of attack, i.e. the difference between pitch angle and flight path angle (Eq. 4).

$$\delta\alpha = \delta\Theta - \delta\gamma = \delta\Theta - \frac{\delta\dot{h}}{V_0} \tag{4}$$

- Atmospheric turbulence does not directly affect the airspeed, i.e. P_{gust} is fully absorbed by the vertical motion of the aircraft.
- The thrust power P_T does not vary.

Equation 1 is linearized around the trim point and is simplified using the above assumptions, such that the dynamic total energy equilibrium becomes Eq. 5. The objective is to add a speed state V to the aircraft state-space model, so Eq. 5 can be rearranged to yield the equations for $\dot{V}$, as shown in Eq. 6. The effect of V on $\dot{h}$ is expressed as the increase in lift due to the change in airspeed, resulting in Eq. 7.

$$mV_0\dot{V} + mg\delta\dot{h} = \frac{\rho S V_0^2}{2}\left(V_0\frac{\partial C_D}{\partial C_L}\frac{\partial C_L}{\partial \alpha}\left(\delta\Theta - \frac{\delta\dot{h}}{V_0}\right) + 2C_D\delta V\right) + P_{gust} \tag{5}$$

$$\dot{V} = -\left(\frac{g}{V_0} - \frac{\rho S V_0}{2m}\frac{\partial C_D}{\partial C_L}\frac{\partial C_L}{\partial \alpha}\right)\delta\dot{h} - \frac{\rho S V_0^2}{2m}\frac{\partial C_D}{\partial C_L}\frac{\partial C_L}{\partial \alpha}\delta\Theta - \frac{\rho S V_0}{m}C_{D,0}\delta V \tag{6}$$

$$\frac{\partial \ddot{h}}{\partial V} = \frac{\rho S V_0}{m}C_{L,0} \tag{7}$$

These expressions can then be directly inserted into the A matrix of the state-space model. The aerodynamic data for $\frac{\partial C_D}{\partial C_L}$, $\frac{\partial C_L}{\partial \alpha}$, $C_{D,0}$, and $C_{L,0}$ is extracted from the results published in [11]. The resulting phugoid mode is stable, with a natural frequency ω_{ph} of approximately 0.01 Hz and a relative damping ξ_{ph} of 0.02, which are reasonable values for such an airplane.

D. Control Surface Actuators

The actuators for all control surfaces are modeled as 2nd-order dynamical systems with symmetrical rate and deflection limits. Equation 8 shows the transfer function between the commanded deflection δ_c and the actual deflection δ. It is defined by its natural frequency ω_{SO}, damping ratio ξ_{SO}, and static gain K_{st}.

$$\frac{\delta}{\delta_c}(s) = \frac{K_{st}\omega_{SO}^2}{s^2 + 2\omega_{SO}\xi_{SO}s + \omega_{SO}^2} \tag{8}$$

By default, the natural frequency for all actuators is set to 10 rad/s, the damping ratio to 0.8, and the static gain to 1. According to [12], a rate limit of ±40 deg/s and a deflection limit of up to ±20 deg are appropriate for an aircraft of this type.

IV. Gust Detection and Estimation

A. Gust and Turbulence Modeling

Atmospheric disturbances are modeled as specified in EASA CS 25.341 [13] and FAR 25 [14] §341. Discrete gusts are modeled as 1-cos vertical uniform gusts, shown here in Eq. 9.

$$U = \frac{U_{ds}}{2}\left(1 - \cos\left(\frac{\pi x}{H}\right)\right) \tag{9}$$

The gust speed profile U thus depends on the 'design speed' U_{ds}, gust gradient H, and gust penetration distance x. Physically speaking, H is half the distance from the beginning to the end of the gust, and varies between 30 ft (9 m) and 350 ft (107 m). U_{ds} is the peak gust velocity, and is specified as:

$$U_{ds} = U_{ref} F_g \left(\frac{H}{350}\right)^{1/6} \tag{10}$$

$$F_g = \frac{1}{2}(F_{gz} + F_{gm}) = \frac{1}{2}\left(\left(1 - \frac{h_{mo}}{250,000}\right) + \sqrt{\frac{MZFW}{MTOW}}\tan\left(\frac{\pi}{4}\frac{MLW}{MTOW}\right)\right) \tag{11}$$

Reference speed U_{ref} decreases with altitude, decreasing linearly from 17.07 m/s EAS at sea level to 13.41 m/s EAS at 15,000 ft, and to 6.36 m/s EAS at 60,000 ft. For the CRM-FERMAT model, the Maximum Zero-Fuel Weight ($MZFW$) and the Maximum TakeOff Weight ($MTOW$) are taken from Table 1. The remaining values are approximated by comparison with the Boeing 777-200 [15], such that the Maximum Landing Weight $MLW = 200{,}000$ kg and the maximum operating altitude $h_{mo} = 43{,}000$ ft.

Continuous turbulence is instead defined by the normalized Von Kármán power spectral density for vertical turbulence, as in Eq.12, and a limit turbulence intensity U_σ.

$$\phi(\Omega) = \frac{L}{\pi}\frac{1 + \frac{8}{3}(1.339\Omega L)^2}{\left[1 + (1.339\Omega L)^2\right]^{\frac{11}{6}}} \tag{12}$$

$$U_\sigma = U_{\sigma,ref} F_g \tag{13}$$

Where the reduced frequency $\Omega = \frac{\omega}{V}$, turbulence scale length $L = 2{,}500$ ft, and the flight profile alleviation factor F_g is the same as that in Eq. 11. The reference turbulence intensity $U_{\sigma,ref}$ decreases linearly with altitude from 27.43 m/s TAS at sea level to 24.08 m/s TAS at 24,000 ft, and then remains constant at 24.08 m/s up to 60,000 ft.

In simulation, a time-series turbulence stream is generated according to the recommendations of AMC 25.341(d) [13]. It is modeled as a Gaussian pseudo-random signal with a root-mean-square wind speed $U_{RMS} = 0.4U_\sigma$.

B. Lidar System

The wind field ahead of the aircraft is measured with a Doppler Wind Lidar. As indicated by the name, such sensors utilize the Doppler effect which describes a frequency shift of any observed wave when emitter and receiver (i.e. observer) of the wave are moving with respect to each other. The idea is to measure the disturbance shortly before encountering it (typically 60-300 m ahead of the aircraft) and to counteract it. This type of lidar should not be confused with lidar systems that aim at detecting the presence of turbulence well in advance (several kilometers) in order to avoid the area. For the remainder of this paper, the term lidar will specifically mean Doppler wind lidar, as this is the sensor type for the present use case of gust load alleviation.

In the considered case, a short pulse (typically lasting for a few tens of nanoseconds) of laser light is emitted. The laser beam has a very low divergence, which allows the illumination of only a specific area ahead of the aircraft. The pulse of light advances along the laser direction, and at each location a tiny fraction of this pulse is scattered by the molecules of the air (and possibly some aerosols if present). The frequency of the light scattered back to the lidar sensor can be compared to that of the light that has been emitted. A shift toward higher frequencies (so-called blue shift) signifies that the sensor and the aerosols/molecules that scattered the light back were moving toward each other. Likewise, if they were moving away from each other, the spectrum is shifted towards lower frequencies (red shift).

If the presence of aerosols can be assumed, so-called coherent heterodyne detection principles with a laser source in the infrared domain are generally the best choice. However, for the alleviation of clear air turbulence at high altitudes

(possible lack of sufficient aerosol concentration) and if a high availability of the remote wind measurement is desired, a so-called direct detection principle with a laser source in the ultraviolet domain can be used, since it can work with so-called Rayleigh-scattering on air molecules. More information on the remote wind measurement technologies and their respective capabilities can be found in the literature, for instance in [3, 16] and references therein.

When using Doppler lidar sensors, only the relative wind component in the direction of the laser beam is measured. If the wind is measured at locations ahead of the aircraft, then the direction of the laser beam (also called line-of-sight, LOS) is almost collinear with the flight path, and the measured relative wind speed is determined mostly by the true airspeed (TAS). On the other hand, the primary information of interest is the vertical wind speed due to its direct effect on the lift, which has to be reconstructed from the relative wind measurements. A way to estimate or reconstruct the missing information (other velocity components as well as the wind at locations that were not directly measured) is to measure the wind at locations with various vertical and lateral offsets with respect to the airplane flight path. Figure 1 shows how the scan geometry creates these offsets by pointing the sensor's LOS off-center with angle a_{scan} and rotating it around the aircraft's longitudinal axis. The resulting LOS directions are not (all) collinear anymore, and an analysis of the differences between the different sensor readings permits the estimation of the transversal components (lateral and vertical) of the wind. This method implicitly assumes that the wind is homogeneous between the points where the measurements are made. This assumption is of course difficult to validate and strongly depends on the current atmospheric conditions encountered by the aircraft.

If measurements are located close to each other, this assumption is valid, but the lateral/vertical distance cannot be reduced infinitely: a reduction of distance corresponds to a reduction of angles between the individual LOS directions, leading to very small differences of the LOS velocities being measured. Consequently, this means that the signal-to-noise ratio (the signal being the difference due to the wind transversal components and the noise being linked to the noise on each measurement) decreases significantly when calculating the difference between measurements taken in near-collinear directions. Hence a trade-off will have to be made between the validity of the homogeneity assumption (linked to the distance of the measurements from the flight path) and the signal-to-noise ratio for the reconstructed transversal wind components.

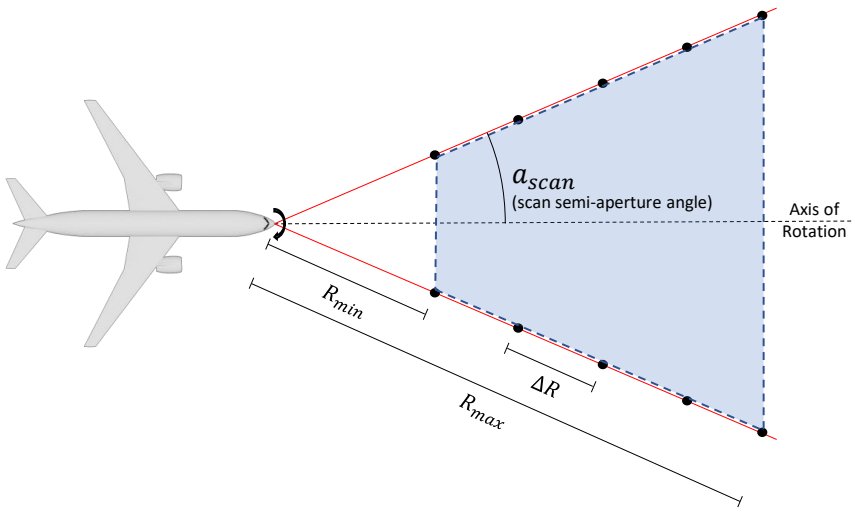

Fig. 1 Lidar scan geometry.

1. Lidar surrogate model

The lidar simulation model, herein called *lidar surrogate model*, constitutes a set of simple analytical equations and a number of carefully chosen and validated variables for determination of the wind speed measurement noise level, i.e. the statistical distribution of individual measurements. This distribution, quantified by the variance σ_v^2 of wind speed measurements, is the key gauge of the lidar performance, and is derived from design variables such as emitted laser power, optical antenna size, measurement distance, and spatial and temporal resolution; the environment of operation

(i.e. flight altitude and atmospheric conditions); and the quality and physical limitations of its technical implementation. As we will see below, this lidar model may be separated into these three domains of variables. This should clarify the use of this model for highlighting (1) the skill level of lidar design and manufacturing, (2) the area/altitude of operation, and (3) the investments or concessions one is ready to take (e.g., in laser power or measurement resolution).

This model is the basis of a somewhat more comprehensive "end-to-end" lidar model of one specific implementation of a Direct-Detection Doppler Wind Lidar (DD-DWL) prototype, realized and continuously augmented at DLR [17] and [18]. Despite not (yet) including all physics (such as photon paths), it notably contains [19] a statistical means (Monte-Carlo-like) for simulation of different noise processes (e.g., electronics, optical speckles), physics of the Doppler spectral analyzer, and in particular the very wind determination algorithm (i.e., Doppler spectral shift) employed in the above mentioned real lidar. Due to this complexity, the end-to-end model is computationally demanding and is hence not suitable to be used directly in the aircraft simulation. Therefore, we prefer to use a simple surrogate model composed of a set of analytical equations. The validity of using this simple model as a "surrogate" (hence this designation) was confirmed by comparison of actual physical lidar wind measurements (with the aforementioned prototype and a reference lidar) with the precision forecast by the end-to-end and surrogate simulators [20].

The surrogate model is based on a very fundamental and generic formulation of the spectral discrimination "error" of a non-specific "spectral analyzer", which is thus applicable to any device determining a spectrum of Gaussian shape by means of spectral channels. The "Cramér-Rao lower bound" (CRLB) on the variance of a Gaussian spectrum estimation by an ideal spectral analyzer (ISA) equipped with an infinite number of channels reads [21] or [22]:

$$\varepsilon^2_{CRLB_{ideal}} = \frac{w^2_{spec}}{N} \tag{14}$$

with w_{spec} being the spectrum's half-width at the $1/e^{1/2}$ point, and N the number of photons, or in our case rather the number of photo-electrons used for the estimation. For the purpose of Doppler wind lidars, we may transform this into (wind) speed variables, thus the CRLB on the speed estimate v reads:

$$\varepsilon_{v_{ideal}} = \frac{w_{RB}}{\sqrt{N_e}} \tag{15}$$

where w_{RB} is the corresponding half-width of the Rayleigh-Brillouin atmospheric backscattered spectrum (however neglecting departure from Gaussian due to Brillouin scattering etc.):

$$w_{RB} = \sqrt{\frac{k_B \cdot T(h)}{m_{air}}} \tag{16}$$

with k_B the Boltzmann constant, $T(h)$ the prevailing air temperature at altitude h, m_{air} the molecular mass of air, and N_e the number of photo-electrons generated on the detector (determined by Eq. 19 below).

The optical spectrum to be analyzed has a large width of some GHz due to the temperature-dependent Brownian motion of the molecular scatterers, resulting in some hundred m/s in speed, as opposed to only a few m/s when relying only on aerosol backscatter (only sufficiently available at lower altitudes, as noted above IV.B).

For realistic physical spectral analyzers (not disposing of an infinite number of spectral channels, i.a.), such as interferometers, a correction factor $\kappa_{v_{real}}$ has to be applied. This penalty factor can be derived by a rigorous mathematical treatment of the actual physical architecture, e.g., as laid out in [23].

There are a number of such possible technical architectures, stemming from different interferometer types and setups, such as Fabry-Perot interferometers in the double-edge setup e.g., [24], quadri-channel Mach-Zehnder setups [22], [25] or double-channel Michelson setups [17], [18], which display diverse correction (or penalty) factors and even more different advantages and disadvantages, both depending on application and requirements. However, the range of the related penalty factor κ_{real} is relatively narrow, ranging from approx. 2.3 to 4.4 [19].

$$\kappa_{real} = \frac{\varepsilon_{v_{real}}}{\varepsilon_{v_{ideal}}} = 2.3 \ldots 4.4 \tag{17}$$

The actual penalty factor obtained thereby is mainly a function of the prevailing conditions (atmosphere: spectral bandwidth, aerosol backscatter ratio) and interferometer-related variables (such as phase sensitivity, global contrast and instrument contrast), the latter parameters being carefully optimized to the former. For the simulator we assume here a (near-)optimal choice of architecture with $\kappa_{real} = 2.3$. Furthermore, the real implementation admittedly seldom achieves the theoretically prognosed performances due to technical issues, trade-offs, etc. Therefore, one has to introduce a

further performance-degrading factor that we may denote as "technology implementation factor" TIF. A value for this is rather speculative; the latest DLR implementation, which is not optimized as it is only for demonstration, yields 1.7 [20], so one may stipulate that for an optimized system:

$$\kappa_{\mathrm{TIF}} = 1.3 \tag{18}$$

So, the expected minimum standard deviation of a wind measurement (please note: in line-of-sight, LOS) with such an interferometric spectral analyzer may be given by:

$$\sigma_{v_{real}} = \varepsilon_{v_{real}} = \kappa_{real} \cdot \kappa_{\mathrm{TIF}} \cdot \left(\frac{k_B \cdot T(h)}{m_{air} \cdot N_e} \right)^{1/2} \tag{19}$$

The next step consists in the derivation of the number of photo-electrons usable for the analysis of the spectrum, i.e. the number of generated photo-electrons generated by the lidar detector(s) due to the impingement of the backscattered photons collected and conditioned by the lidar optics.

For this purpose we use the "lidar-equation" from textbooks (e.g., [26]) and determine the received optical power P_{Rx}, the thus generated relevant photo-current i_{Rx} at the detector(s)' output and the according photo-electron number $N_{e,Rx,ss}$ for a single laser shot (index ss):

$$P_{Rx} = \frac{\eta_{opt} \cdot c \cdot \beta_{atm}(h,\lambda) \cdot T_{atm}(R,h,\lambda) \cdot E_p \cdot A_{Rx}}{2R^2} \tag{20}$$

$$i_{Rx} = P_{Rx} \cdot \rho_{\mathrm{det}} \tag{21}$$

$$N_{e,Rx,ss} = \frac{i_{Rx} \cdot \Delta t_s}{e} = \frac{2\, i_{Rx} \cdot \Delta R}{e \cdot c} \tag{22}$$

with η_{opt} the optical efficiency of the lidar system (mainly receiving part), c the speed of light, β_{atm} and T_{atm} the atmospheric backscatter and transmission, respectively, depending on the altitude h, the wavelength λ of the used laser and the traversed range R up to the target distance; the latter, T_{atm}, however, may be neglected to unity for the short distances we consider for the GLA use case; E_p is the power of a single emitted laser pulse and A_{Rx} the lidar receiving aperture; ρ_{det} signifies the detector's quantum efficiency for the conversion of photons into electrons; e is the electron charge; and Δt_s is the system's sampling time that may be transformed into the range resolution $\Delta R = c/2 \cdot \Delta t_s$.

The high demand in signal (and signal-to-noise ratio SNR) due to the broad spectrum to be evaluated usually requires the collected signal information of several laser shots to be aggregated to an average. This may be done in post-processing (digital), as in the authors' prototype [18] but potentially also directly within the detector (analog), as in past and present airborne (AWIATOR) and spaceborne (AEOLUS) direct-detection UV wind lidars [27] and, [28]. The electron number available for the spectrum estimation of Eq. (19) may thus be extended to $N_{e,Rx,av}$ (index av for average) with a certain number of measurements:

$$N_{e,Rx,av} = N_{e,Rx,ss} \cdot n_{meas} \tag{23}$$

This number may instantly be replaced by the following ratio of the laser pulse repetition rate PRF and the required refresh rate $r_{refresh}$, i.e. the rate at which the wind measurements are collected by the wind estimation algorithm of Section (IV.C).

$$n_{meas} = \frac{PRF}{r_{refresh}} \tag{24}$$

Last, we introduce the power-aperture-product PAP, a common measure for sizing lidar systems. It basically represents the trade-off between realistic and affordable laser power $P_{Tx} = E_p \cdot PRF$ and reasonable and also affordable receiver telescope size A_{Rx} (e.g., due to aircraft integration constraints), both being equivalent in the above lidar-equation:

$$PAP = P_{Tx} \cdot A_{Rx} = E_p \cdot PRF \cdot A_{Rx} \tag{25}$$

PAP may lead to reasonable estimates on the other important, more engineering-technical design quantity S.W.a.P. (size, weight and electrical power) of the lidar system (laser and receiver systems).

We are now able to collapse the whole of the above equations into a single one for the standard deviation of an averaged wind speed measurement:

$$\sigma_{v,av} = \frac{\kappa_{real}\ \kappa_{\mathrm{TIF}}}{\left(e \cdot \eta_{opt} \cdot \rho_{det}\right)^{1/2}} \left(\frac{k_B \cdot T(h)}{m_{air} \cdot \beta_{atm}(h,\lambda)}\right)^{1/2} \left(\frac{R^2 \cdot r_{refresh}}{PAP \cdot \Delta R}\right)^{1/2} \tag{26}$$

This expression can be separated into three distinct terms:

- The first term represents the Doppler wind lidar technical architecture and implementation. For the simulation of Chapter (VI) it remains constant for given (typical) lidar performance values. Even though these values have a certain claim of universality, they have to be carefully assessed by lidar designers depending on the actual direct-detection Doppler lidar technique to be employed.
- The second term, the atmospheric contribution, is constant for a given flight altitude h. Since for realistic (and worst-case) estimations a pure molecular atmosphere may and should be considered, the backscatter coefficient β_{atm} collapses into a mere function of the atmospheric temperature T that in turn may be determined by a certain model atmosphere (e.g., International Standard Atmosphere ISA). Hereby, the spread in the models does not contribute significantly to the final outcome.
- The third term contains the system design variables that may be adopted to meet the requirements of the wind reconstruction algorithm to retrieve the LOS wind speed with a certain precision. In short, the possible wind speed precision scales with the requirements in linear and square-root proportions:

$$\sigma_{v,av} \propto R\sqrt{\frac{r_{refresh}}{PAP\ \Delta R}} \tag{27}$$

Here, the PAP is of central interest for the lidar designer since it represents the ultimate (size and power) scale of the lidar instrument. Longer range gates ΔR are favorable in terms of photon budget, but may hamper the retrieval of relevant gust scales by the wind field estimation algorithm (WFE). The needed refresh rate $r_{refresh}$ of synthetic measurements (averages) has to be analyzed within the performance evaluation of the WFE as well. Distance R has the biggest impact on the performance; above a certain level, it soon does not make any more sense to deliberately incorporate noisy measurements into the WFE.

2. Implementation

The lidar model is implemented as a C++ library which is encapsuled in a Simulink S-function. The code is fully compliant with C++ 98, with the exception of the random value generation for the measurement noise, which uses the C++ 11 random library. The S-function is compatible with all versions of Simulink tested by the authors (R2007b to R2019a) and is provided in separate versions for 32 bit and 64 bit architectures. In case of any compatibility problems, submit an issue on the repository mentioned in Section II.

C. Wind Field Estimation

The goal of the wind reconstruction is to interpret the line-of-sight wind velocity measurements made and to deduce the most likely wind field that could have caused these measurements. The first three rows of Fig. 2 illustrate this process.

The estimated wind field is an evenly-spaced set of nodes parametrized by a lead time τ_{lead} and a lag time τ_{lag}. Mathematically, the wind reconstruction is a maximum likelihood problem: it determines the wind velocities at the estimation mesh nodes which yield the optimal fit (in the least-squares sense) to the obtained measurements. Each measurement is weighted by its corresponding standard deviation to prioritize more accurate measurements (those with a low standard deviation) over less accurate measurements. Additionally, a Tikhonov regularization [29, 30] is included in the optimization problem to ensure a certain degree of smoothness in the resulting estimated wind field. The detailed equations and the mathematical derivation of the wind reconstruction algorithm are found in [31].

Least-squares optimization problems such as the wind reconstruction algorithm discussed here can be solved using various nonlinear optimization methods. In the presented case, the Gauss-Newton method is used; since the Jacobian matrix (i.e., sensitivity matrix of the residuals w.r.t. the estimated wind speeds) does not depend on the estimated wind vector and the residual vector linearly depends on the estimated wind vector, the Gauss-Newton algorithm will find the optimal solution after a single iteration, regardless of the initial estimate [31].

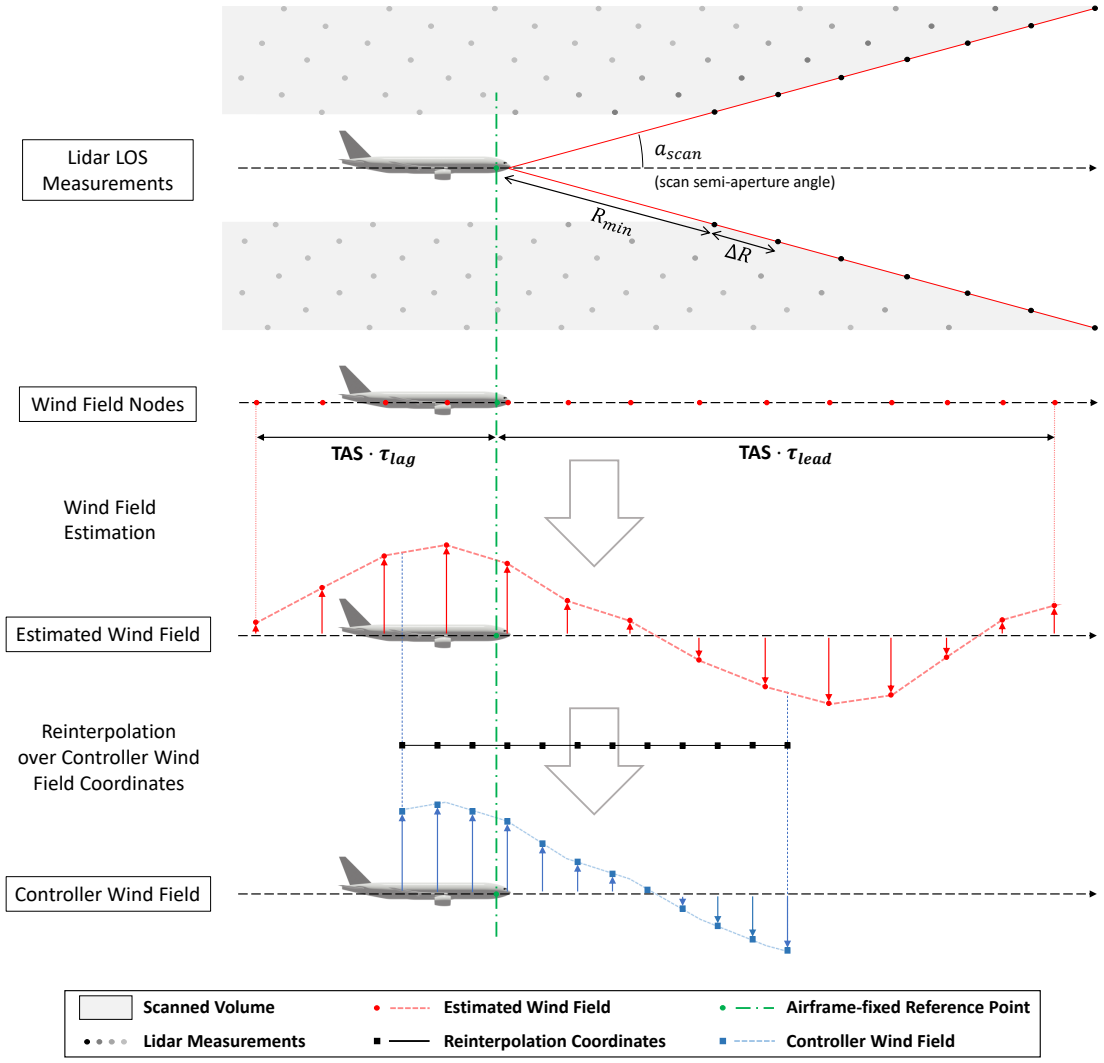

Fig. 2 Wind estimation process, from lidar measurements to controller wind field.

V. Lidar-Based Gust Load Alleviation

Compared to legacy methods of gust detection, i.e. some kind of angle-of-attack sensor near the nose, a wind field obtained by a lidar sensor presents several advantages for load alleviation control.

Firstly, with a potential effective range of over 100 m, the available lead time is much greater. Note that the effective range is smaller than the maximum measurement distance of the lidar in line-of-sight direction, as the line-of-sight is not collinear with the flight path and various measurements need to be combined to provide a valid wind estimate (see sections IV.B and IV.C). A large commercial aircraft like the CRM at cruise conditions has a true air speed on the order of 250 m/s and a distance of approximately 25 m between the nose and the leading edge of the wing. Assuming the lidar sensor and the angle-of-attack sensor are both located at the nose, the lidar can detect turbulence 0.5 seconds before it reaches the wing, compared to about 0.1 seconds for the angle-of-attack sensor. When taking into consideration various system delays, the difference becomes even more evident.

Secondly, the estimated wind field can be treated using data processing techniques which would otherwise be infeasible. For instance, in [32], wavelet-based filtering techniques are used to separate the wind field according to frequency bands and amplitude. Each of the resulting signals is then exploited with an appropriate control strategy; elevator inputs were only used on the low-frequency high-amplitude channel and spoilers only used on the mid-frequency high-amplitude channel, i.e. effectively preventing by design any spoiler activity for small-amplitude gusts.

Finally, the wind field can be sampled at any position in the estimated range. Seeing as it can extend both ahead and behind the aircraft, the control designer can freely choose the location or time-difference of the wind inputs to the control law. Locations ahead of the aircraft are clearly useful, but the positions of the principal aerodynamic surfaces, possibly with an offset to account for system delays, can also be useful.

The lower part of Fig. 2 illustrates this sampling. The positions sampled for the controller wind field are defined as a vector of time-differences relative to the airframe-fixed point, shown here in black with square dots. In this figure, the controller wind field is a regularly-spaced subsection of the estimated wind field, but this is not obligatory. The choice, quantity, and order of time-coordinates in this vector are not restricted in any way, although it is not advisable to sample points beyond the estimated range.

The controller wind field is thus created by linearly interpolating the estimated wind field at the points specified in this vector. To account for the difference in sampling rates between the wind field estimation algorithm and the controller (see section VI), the controller wind field is reinterpolated at the controller's sampling frequency, i.e. 100 Hz. Each time it is reinterpolated, the position of the airframe-fixed reference point is updated with the current position of the aircraft. Intuitively speaking, this means that the controller wind field coordinates "slide" forward along the estimated wind field as the aircraft continues moving between the two timesteps.

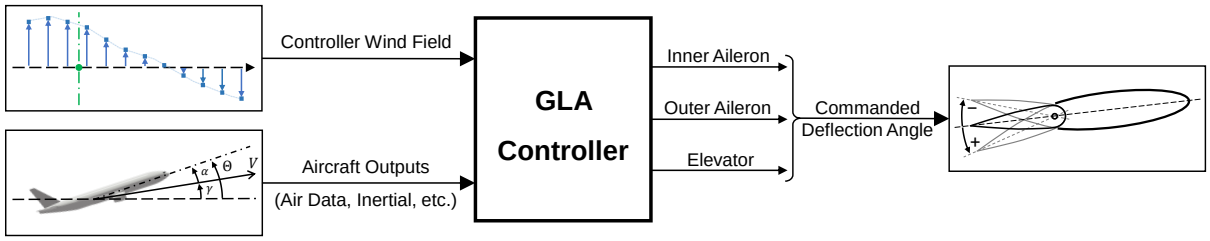

Fig. 3 Gust load alleviation controller interface with the wind reconstruction system, aircraft sensors, and control surfaces.

The reconstructed wind field is ideally suited for feedforward control. Feedback gust load alleviation controllers, which are usually based on inertial feedback, are well suited to improving the structural dynamics, e.g. by increasing modal damping. They can be effective at reducing fatigue loads and fairly robust with respect to uncertainties, but producing significant reductions in peak loads is challenging. Feedforward control can instead directly compensate for gust effects on the aircraft, allowing for a strong reduction in peak loads, especially given a long lead time and accurate wind information. It usually does not have a direct effect on system stability, although performance can be very sensitive to uncertainties. Ideally, a complete gust load alleviation function combines both feedback and feedforward controllers to take advantage of the strengths of both. An example of a lidar-based feedforward controller is described in section VIII.

Figure 3 illustrates the interface of the GLA controller with the other principal subsystems. The inputs to the controller include the controller wind field and outputs from the aircraft. These outputs include typical quantities measured by air data and inertial systems, such as angle of attack (α), pitch attitude and rate (Θ and q, respectively), and vertical load factor (n_z), as well as measured system quantities such as control surface deflections. Its outputs consist of deflection commands sent to the (symmetrically actuated) inner and outer ailerons, and the elevator.

VI. Evaluation Using a Hybrid Simulation Architecture

The aircraft model, lidar system, and controller described above are combined in a multirate Simulink model. The architecture of this hybrid model is shown in Fig. 4. The figure is divided in two sections: below the dashed line are the model components implemented directly in Simulink, whereas the upper part is coded in C++ and is included in the model as an S-function (as mentioned in section IV.B.2). This S-function contains the true wind field, lidar system, and wind reconstruction algorithm.

The colors of the various blocks indicate their sampling rate. The physical components, i.e. the aircraft, actuators, and atmosphere, are all simulated as continuous-time systems. The lidar system operates at a sampling rate which is determined by the selected laser PRF, and the wind reconstruction algorithm estimates the wind field at a rate of 10 Hz. The controller and its associated wind field reinterpolation function instead operate at 100 Hz.

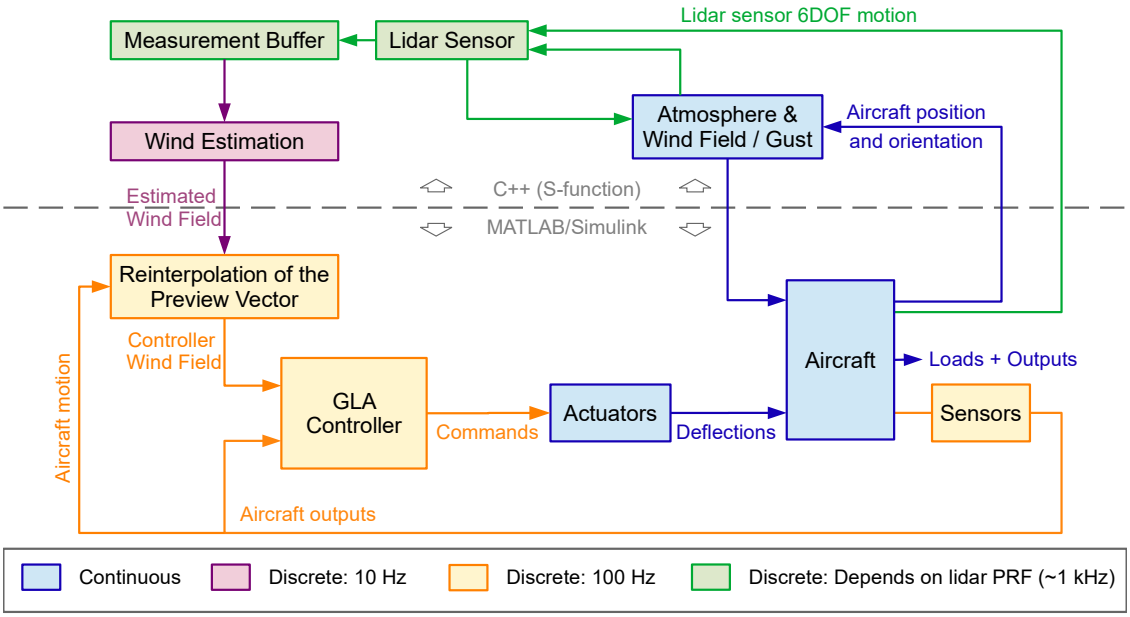

Fig. 4 Architecture of the hybrid simulator

This kind of hybrid simulation model, i.e. with mixed sampling times, is useful and necessary to realistically evaluate the interaction between digital avionics and physical systems. Digital systems function in discrete time, i.e. they accept inputs and provide outputs only at regularly-occurring points in time. Input and output values remain same between these points in time, and the duration of time between them, i.e. the timestep, defines the system's sampling rate.

In a real-time application, as is the case for flight-control avionics, the system is designed to perform the necessary computations within a predefined amount of time, which for a discrete system is equal to a given number of timesteps. This effective sampling rate determines the function's bandwidth, and plays an important role in synchronization among different functions and subsystems. In this case, the unique characteristics of the lidar and wind reconstruction system result in 3 different discrete sampling times interacting with a continuous-time physical system. This hybrid simulation architecture is meant to capture the complex interactions among them, including, for instance, synchronization delays.

Control design is often done in continuous-time, especially if classical methods are used. When implemented in discrete time, a continuous controller which is insufficiently robust for the system's sampling rate may perform poorly, or even become unstable. This is often the case for very high-performance, aggressive continuous-time feedback controllers.

This can be avoided by designing the controller with robustness in mind. In an H_∞ robust control framework, for instance, high-frequency roll-off specifications can be used to avoid excessively aggressive controllers. Alternatively, many control design methods support direct discrete-time synthesis. This inherently guarantees that controller is suitable for a discrete-time implementation, and easily allows extra delay steps to be included to improve the controller's robustness to system delays.

VII. Benchmark Problem

Alongside the model described above, this paper aims to propose a benchmark problem for active gust load alleviation control design. The problem presented here was intended to capture the fundamental considerations taken into account when designing a gust load alleviation function while remaining reasonably simple and clear. In a "real" industry-size design problem, a greater number and complexity of the requirements is to be expected.

Some of the choices and assumptions made here are, at best, educated guesses. Should readers find some aspects of the design problem questionable or unrealistic, suggestions for improvement and feedback are more than welcome.

A. Problem Definition

The full set of requirements (objectives, constraints, and robustness requirements) is listed in Table 2. They are all evaluated across the full discrete gust spectrum and 120 seconds of continuous turbulence (cf. FAA Part 25 / EASA CS25 §341 a and §341 b, and section IV.A). Limit values for discrete gust cases $y_{lim,\S341a}$ are determined from the peak absolute value of the response. For continuous turbulence cases, the limit values $y_{lim,\S341b}$ are calculated by multiplying the limit turbulence intensity U_σ by the ratio of root-mean-square output values to root-mean-square turbulence input $\overline{A}$:

$$y_{lim,\S341a} = \max|y(t)|, \qquad y_{lim,\S341b} = U_\sigma \cdot \overline{A} = U_\sigma \cdot \frac{y_{RMS}}{U_{RMS}} \tag{28}$$

where y represents a generic output value. In most cases, the final limit value is then the maximum of the two: $y_{lim} = \max\left(y_{lim,\S341a}, y_{lim,\S341b}\right)$.

The idea is to enable a reduction in the wing structural mass by reducing the wing loads incurred during gust encounters. As such, the proposed *objective* is to reduce the wing bending loads by 25 % at five load stations along the wingspan, starting at the wing root and ending at 24.5 m from the aircraft centerline, roughly 5 m inboard of the wingtips.

The *constraints* are intended to avoid an increase in the limit loads of the rest of the aircraft structure, to protect the control authority and stability of the flight control system, and to avoid a degradation of the ride quality. The HTP-root bending moment is chosen to cover the first point, as controllers using the elevator tend to generate the most additional loads at the HTP. It is limited to 200 % of the reference envelope to account for the fact that the HTP sizing loads are driven by maneuvering requirements. To guarantee control authority, limit values in continuous turbulence $y_{lim,\S341b}$ of control surface deflections and deflection rates must not exceed 50 % and 80 % of their saturation limits, respectively. For ride quality, two constraints are defined: firstly, the limit incremental load factor must not be greater than the open-loop reference value. Secondly, the maximum Percentage of Ill Passengers (PIP) [33, 34] should not exceed the open-loop values. The PIP is evaluated at the center of gravity and 20 m fore and aft, roughly the front and rear ends of the cabin, and the maximum of these three values is taken.

The gust load alleviation function must also be reasonably robust against a few basic uncertainties, including system delays, actuator dynamics, and lidar parameters. System delays are condensed into a single delay between the control commands and the actuators. Lidar uncertainties are only represented by the Power Aperture Product (PAP), which is the only available parameter that has a direct effect on the lidar system's performance without any complex interactions with other parameters.

For the *robustness requirements*, a range of values is considered for a few key parameters. The nominal scenario requires only a delay of 3 controller cycles, i.e. 30 ms at 100 Hz. In the robustness performance evaluation, a time-invariant uncertain delay up to 80 ms is considered instead. Similarly, variations of actuator characteristics and lidar power aperture product are also considered. All combinations of the uncertain parameters have to be considered, however in this robustness evaluation all actuators share the same characteristics (e.g. inner/outer ailerons and elevators always have an identical dynamic behavior).

Obviously, parameter variations considered in the frame of the robustness investigation are not known a-priori by the controllers, so somehow "gain-scheduling" the controller for the current case is not allowed. Adaptive controllers (either through explicitly estimating these parameters or via direct adaption) can be proposed, but should be identified as such and the adaptation mechanism should be well documented.

B. Reference Load Envelopes

Ideally, to provide a realistic benchmark, the objective values and constraints for the various type of loads and the various locations across the airframe would be defined as improvements with respect to the "open-loop" absolute limit loads.

Unfortunately, for this aircraft model neither the limit loads nor the equilibrium loads are available. A set of reference load envelopes was instead defined based on the open-loop gust load envelope and experience from other models. In the end, the type of criteria used and the defined values are sufficiently representative of a typical gust load alleviation control design problem.

The reference envelope for the vertical bending moment along the wing is shown in Fig. 5. [†]

[†]Numerical values of the envelope and target values shown here may be subject to errors. In the event that future corrections will be necessary, the new values will be directly integrated into the repository linked in the introduction. In case of doubt, the values in the repository should be taken as reference.

Table 2 Requirements of the benchmark problem (objectives, constraints, and robustness requirements)

Objectives		
Variable	**Description**	**Limit value**
WR.OSID.112.MX	Δ Bending moment at right wing root	$\leq 5.68 \cdot 10^6$ Nm
WR.OSID.122.MX	Δ Bending moment at 10 m right wing	$\leq 3.29 \cdot 10^6$ Nm
WR.OSID.130.MX	Δ Bending moment at 14.86 m right wing	$\leq 1.88 \cdot 10^6$ Nm
WR.OSID.138.MX	Δ Bending moment at 19.7 m right wing	$\leq 0.80 \cdot 10^6$ Nm
WR.OSID.146.MX	Δ Bending moment at 24.5 m right wing	$\leq 0.20 \cdot 10^6$ Nm

Constraints		
Variable	**Description**	**Limit value**
HR.OSID.21.MX	Δ Bending moment at right HTP root	$\leq 10.45 \cdot 10^5$ Nm
δe / δa_{inner} / δa_{outer}	Control surface deflections	$\leq 10°$ (§341 b only)
$\dot{\delta} e$ / $\dot{\delta} a_{inner}$ / $\dot{\delta} a_{outer}$	Control surface rates	$\leq 32°/s$ (§341 b only)
Δn_z	Incremental vertical load factor at center of gravity	≤ 0.82 g
PIP_{max}	Maximum Percentage of Ill Passengers	≤ 7.4 ‰

Robustness Requirements			
Variable	**Description**	**Nominal value**	**Uncertainty range**
Δt_{act}	Time delay between controller and actuators	30 ms	20 - 80 ms
ω_{SO}	Control actuator natural frequency	10 rad/s	8 - 12 rad/s
ξ_{SO}	Control actuator damping ratio	0.8	0.65 - 0.95
PAP	Lidar Power Aperture Product	0.05 Wm^2	0.035 - 0.065 Wm^2

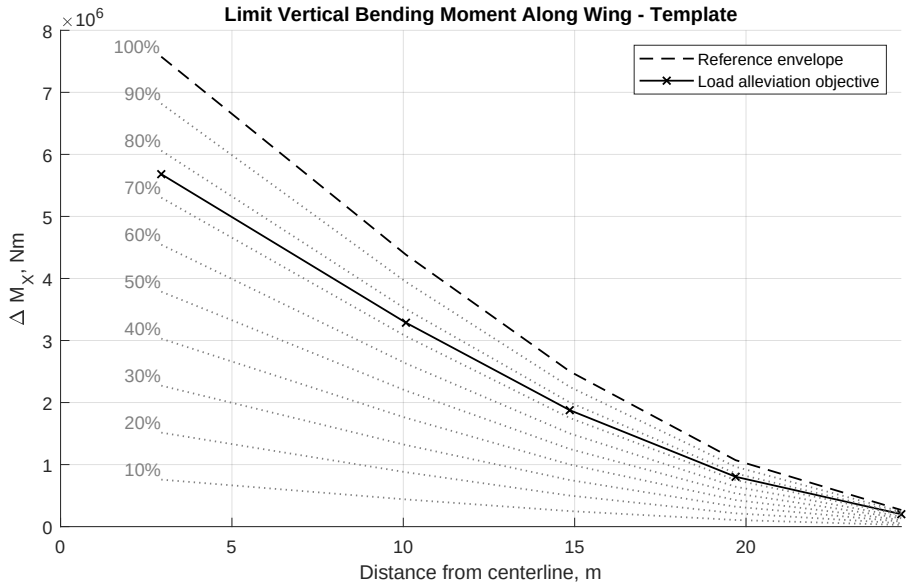

Fig. 5 Limit bending moment moment along the wing. Includes the reference envelope and load alleviation objective specified in the benchmark problem

VIII. Control Design Example

This section presents a basic example of how a lidar-based gust load alleviation controller can be designed and then evaluated against the benchmark problem. The resulting controller is provided as part of the benchmark as the default controller.

A. Design of Default Feedforward Controller

The feedforward control concept used here is a further development of the preview-control methods described in [35]. The wind field input can be modeled as a series of discrete time delays, as in Fig. 6. The controller is then defined as a discrete state-space system with as many inputs as there are delayed wind field signals, and as many outputs as there are available control inputs. In principle, feedback signals can also be included in the controller's inputs, however only a pure feedforward controller is considered here.

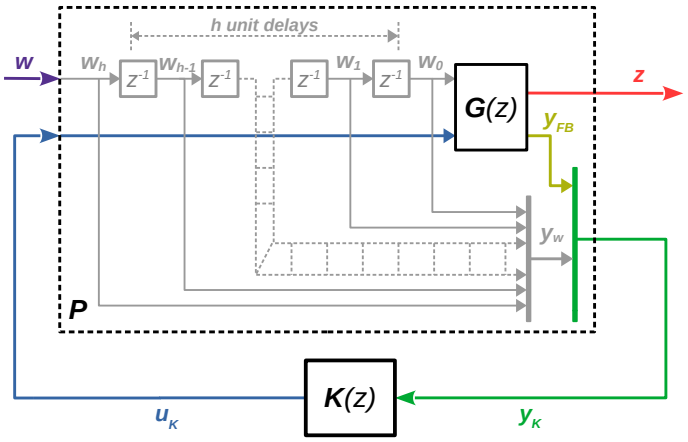

Fig. 6 Discrete wind field approximation for control design

The controller wind field is chosen to include a preview distance of approximately 100 m as well as the entire length of the fuselage. Considering a discrete sampling time of 0.1 s, a true air speed of 260 m/s, and a fuselage length of 62.75 m (see Table 1), it comes out to 40 leading nodes and 25 trailing nodes, which combined with the base node result in a 66-step controller wind field. All three available control inputs are used, i.e. elevator, symmetrical inner ailerons, and symmetrical outer ailerons. The controller is thus chosen as a simple gain matrix with 3 rows and 66 columns.

The transfer between vertical wind and wing root bending moment is shown as a continuous black line in Fig. 7. The frequency band below 2 Hz contains the majority of the response, most of which lies within the available actuator bandwidth. Within this band, the first peak around 0.4 Hz corresponds to the short-period mode, whereas the peak around 1.35 Hz is the first wing-bending mode.

A weighted H_2 tuning requirement was chosen for the wing root bending moment. The weighting function is based on the Von Kármán continuous turbulence model specified in the certification requirements, and is expressed using the approximate filter from [36]. It also includes a low-pass filter to reduce the weight of the higher-frequency components and to ensure that the targeted frequency band is within the actuators' bandwidth. The dotted curve in Fig. 7 shows the weighted magnitude of the wing root bending moment transfer.

Constraints on actuator dynamics were instead expressed using H_∞ requirements. For all three actuators, a 20 dB/decade roll-off is specified starting at 2 Hz. The inner and outer ailerons, also have an additional roll-on specification to avoid excessive deflections for longer gusts.

The 'full' feedforward control law thus obtained is shown in blue in Figs. 7 and 8. Figure 7 shows a strong reduction in loads below 2 Hz, as well as a significant reduction in the peak just below 3 Hz. The time-domain responses reveal a 75 % reduction in peak wing root bending loads. This level of performance requires aileron deflections slightly greater than ±10 deg and deflection rates around 100 deg/s, as well as peak HTP-root bending moments over 400 % greater than the open-loop values.

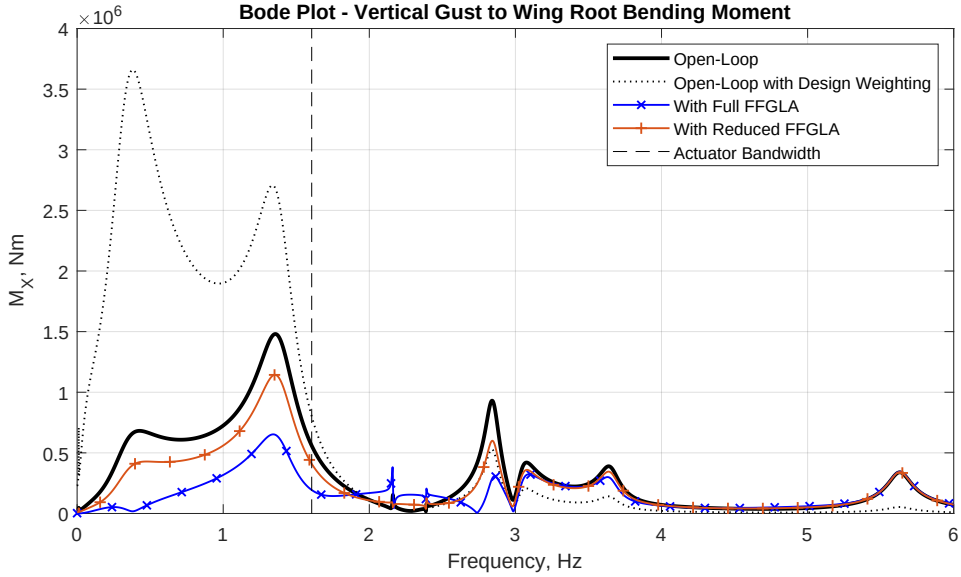

Fig. 7 Magnitude of the transfer function between the vertical gust velocity and the wing root bending moment for the open-loop aircraft, the H_2 design weighting, the full feedforward law, and the reduced feedforward law, as well as the cutoff frequency of the control actuators.

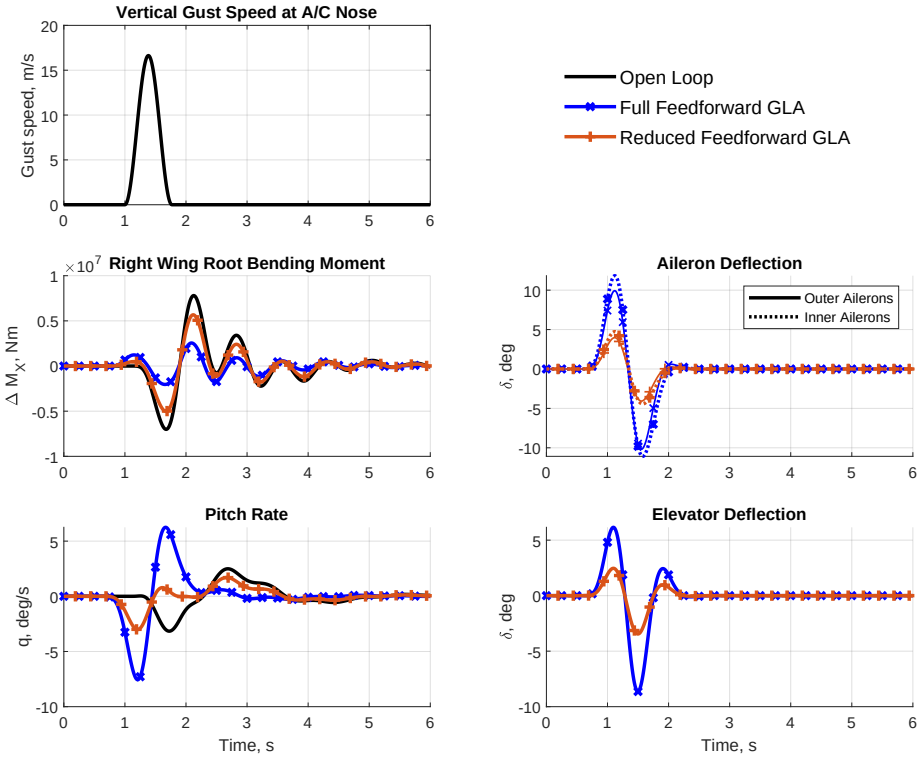

Fig. 8 Time-domain response of the aircraft to a 100 m discrete gust in open-loop, with the full feedforward law, and with the reduced feedforward law, assuming a perfect estimation of the wind field.

This law is clearly too aggressive: it exceeds the objectives and constraints specified in Table 2 as well as the actuator rate limits. Seeing as a feedforward law does not directly affect the stability or internal dynamics of the system, it can be scaled or filtered fairly easily. In this case, a simple gain on all the control inputs has a nearly linear effect on peak values. This scaling gain is chosen to comply with the deflection rate limits in section III.D. Seeing as the peak deflection rate among all the actuators is 100 deg/s on the inner ailerons, the gain is chosen as 0.4. This 'reduced' law is plotted in orange in Figs. 7 and 8.

Known delays are automatically compensated by shifting the controller wind field coordinates forward. The shift is calculated by multiplying the delay by the true airspeed.

B. Evaluation against Benchmark Problem

The wing bending moment along the wing span for both benchmark problem scenarios is shown in Fig. 9, and Table 3 contains the limit values of the constrained variables.

Table 3 Limit values of constrained variables

Constraints			
Variable	Limit	Nominal	Robust
HR.OSID.21.MX	$10.45 \cdot 10^5$ Nm	$6.32 \cdot 10^5$ Nm	$8.55 \cdot 10^5$ Nm
δe	10°	2.15°	2.70°
δa_{inner}	10°	4.23°	4.79°
δa_{outer}	10°	3.91°	4.47°
$\dot{\delta} e$	32°/s	15.2°/s	21.1°/s
$\dot{\delta} a_{inner}$	32°/s	20.5°/s	25.9°/s
$\dot{\delta} a_{outer}$	32°/s	19.9°/s	25.5°/s
Δn_z	0.82	0.52	0.59
PIP_{max}	7.4 ‰	4.64 ‰	5.29 ‰

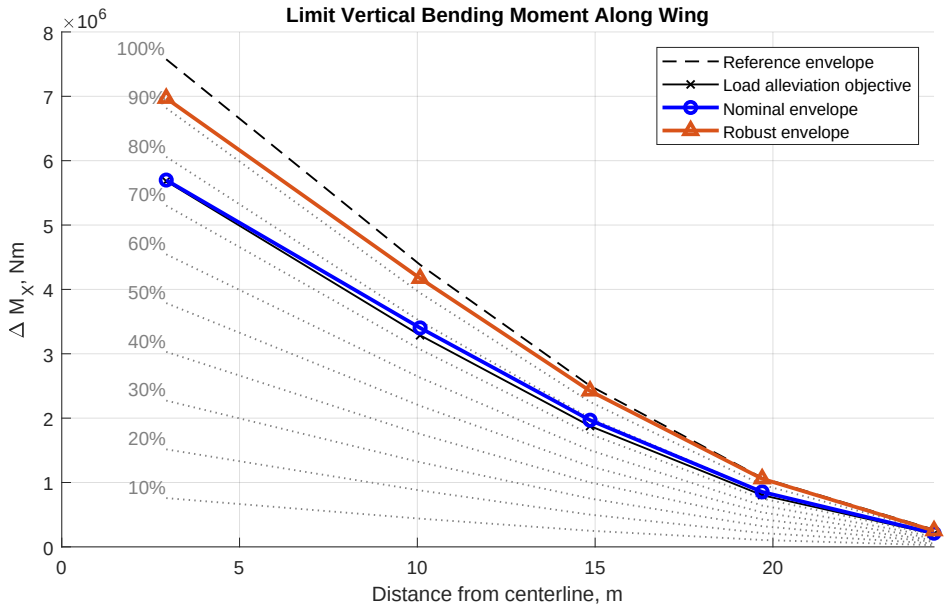

Fig. 9 Nominal and Robust wing vertical bending moment envelopes of the controller example.

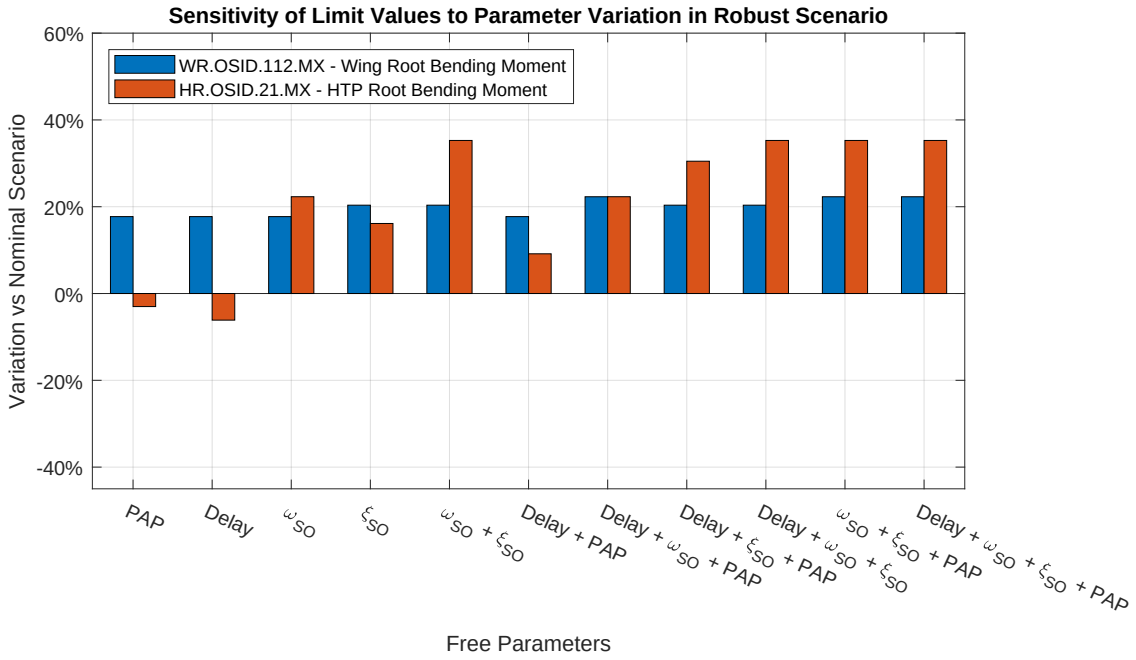

Fig. 10 Sensitivity of the wing and HTP loads to the parameters specified in the robustness requirements. Combinations of parameters listed along the x-axis are allowed to vary to their limits while the rest are kept at their nominal values.

The nominal performance nearly meets the objective, with a reduction of just under 25 % in wing bending loads and no violation of the constraints. The robust scenario instead results in only around 9 % reduction in wing bending moment at the wing root decreasing to none on the outer wing, however it meets all constraints.

The sensitivity of wing root bending moment and HTP-root bending moment to the various robustness parameters can be observed in Fig. 10. A closer examination reveals that while the large loss in performance is caused by a variety of factors, the increase in HTP loads can be traced mainly to the variations in actuator dynamics. The actuator damping ratio ξ_{SO} and natural frequency ω_{SO} clearly drive the HTP loads and have a fairly important effect on the wing loads, however this occurs at opposite extremes in parameter values. A reduction in damping increases actuator overshoot, raising elevator loads, whereas an increase in damping slows the response, limiting actuator bandwidth and reducing the performance of the load alleviation law. Natural frequency ω_{SO} has a similar effect.

IX. Summary and Outlook

This paper presents a public benchmark for lidar-based active gust load alleviation based on the Common Research Model. This includes a linear aeroservoelastic model of the CRM-FERMAT configuration, a lidar-based gust detection system, and a sample feedforward controller, as well as the necessary functions and scripts for simulation. It also defines a benchmark problem, proposed as a design challenge for the community. The authors hope that this benchmark will encourage community engagement, and welcome new features and controllers shared by members of the community.

X. Acknowledgments

The authors would like to acknowledge the funding from the German Research Foundation (Deutsche Forschungsgemeinschaft / DFG) and the European Commission.

The benchmark definition and assembly was made by the first author, whose PhD thesis is funded by German Research Foundation (DFG) under German's Excellence Strategy - EXC 2163/1- Sustainable and Energy Efficient Aviation - Project-ID 390881007. The development of some components of the benchmark (e.g. the Loewner-framework-based aeroelastic modeling of the CRM, the lidar sensor model, and wind reconstruction algorithm) and the work of the other authors has been funded within the framework of the European CleanSky Joint Technology Initiative – Smart Fixed Wing Aircraft (Grant Agreement Number CSJU-GAM-SFWA-2008-01) and is currently being pursued within the framework of the European CleanSky2 Joint Technology Initiative – Airframe (Grant Agreement Number CS2JU-AIR-GAM-2014-2015-01 Annex 1, Issue B04, October 2nd, 2015) being part of the Horizon 2020 research and innovation framework programme of the European Commission.

The authors also would like to acknowledge NASA and Boeing's contribution in the form of the Common Research Model.

References

[1] Regan, C. D., and Jutte, C. V., "Survey of Applications of Active Control Technology for Gust Alleviation and New Challenges for Lighter-weight Aircraft," Tech. Rep. NASA/TM—2012–216008, NASA, Dryden Flight Research Center, Edwards, California, Apr. 2012.

[2] Hahn, K.-U., and Koenig, R., "ATTAS flight test and simulation results of the advanced gust management system LARS," *Guidance, Navigation and Control Conference*, American Institute of Aeronautics and Astronautics, Hilton Head Island,SC,U.S.A., 1992. https://doi.org/10.2514/6.1992-4343, URL https://arc.aiaa.org/doi/10.2514/6.1992-4343.

[3] Schmitt, N. P., Rehm, W., Pistner, T., Diehl, H., Navé, P., Jenaro-Rabadan, G., Mirand, P., and Reymond, M., "Forward Looking Clear Air Turbulence Measurement with the AWIATOR LIDAR Sensor," Berlin, 2007, pp. 179–184.

[4] Fezans, N., Schwithal, J., and Fischenberg, D., "In-flight remote sensing and identification of gusts, turbulence, and wake vortices using a Doppler LIDAR," *CEAS Aeronautical Journal*, Vol. 8, No. 2, 2017, pp. 313–333. https://doi.org/10.1007/s13272-017-0240-9, URL http://link.springer.com/10.1007/s13272-017-0240-9.

[5] Fezans, N., Vrancken, P., Linsmayer, P., Wallace, C., and Deiler, C., "Designing and Maturating Doppler Lidar Sensors for Gust Load Alleviation: Progress Made Since AWIATOR," Bordeaux, France, 2020.

[6] Giesseler, H.-G., Kopf, M., Varutti, P., Faulwasser, T., and Findeisen, R., "Model Predictive Control for Gust Load Alleviation," *IFAC Proceedings Volumes*, Vol. 45, No. 17, 2012, pp. 27–32. https://doi.org/10.3182/20120823-5-NL-3013.00049, URL https://linkinghub.elsevier.com/retrieve/pii/S1474667016314239.

[7] Galffy, A., Gaggl, R., Mühlbacher, R., Frank, D., Schlarp, J., and Schitter, G., "Turbulence load prediction for manned and unmanned aircraft by means of anticipating differential pressure measurements," *CEAS Aeronautical Journal*, 2021. https://doi.org/10.1007/s13272-021-00512-y, URL http://link.springer.com/10.1007/s13272-021-00512-y.

[8] Vassberg, J., Dehaan, M., Rivers, M., and Wahls, R., "Development of a Common Research Model for Applied CFD Validation Studies," *26th AIAA Applied Aerodynamics Conference*, American Institute of Aeronautics and Astronautics, Honolulu, Hawaii, 2008. https://doi.org/10.2514/6.2008-6919, URL https://arc.aiaa.org/doi/10.2514/6.2008-6919.

[9] Klimmek, T., "Parametric Set-Up of a Structural Model for FERMAT Configuration for Aeroelastic and Loads Analysis," *Journal of Aeroelasticity and Structural Dynamics*, , No. 2, 2014, pp. 31–49. https://doi.org/10.3293/asdj.2014.27, URL https://doi.org/10.3293/asdj.2014.27.

[10] Quero, D., Vuillemin, P., and Poussot-Vassal, C., "A Generalized State-Space Aeroservoelastic Model Based on Tangential Interpolation," *Aerospace*, Vol. 6, No. 1, 2019, p. 9. https://doi.org/10.3390/aerospace6010009, URL http://www.mdpi.com/2226-4310/6/1/9.

[11] Sclafani, A., DeHaan, M., Vassberg, J., Rumsey, C., and Pulliam, T., "Drag Prediction for the NASA CRM Wing-Body-Tail Using CFL3D and OVERFLOW on an Overset Mesh," *28th AIAA Applied Aerodynamics Conference*, American Institute of Aeronautics and Astronautics, Chicago, Illinois, 2010. https://doi.org/10.2514/6.2010-4219, URL https://arc.aiaa.org/doi/10.2514/6.2010-4219.

[12] "Aviation Safety and Pilot Control: Understanding and Preventing Unfavorable Pilot-Vehicle Interactions," Tech. rep., National Research Council, Washington, D.C., 1997.

[13] EASA, *CS-25 Amendment 26: Certification Specifications and Acceptable Means of Compliance for Large Aeroplanes*, 2020. URL https://www.easa.europa.eu/document-library/certification-specifications/cs-25-amendment-26-0.

[14] FAA, *CFR Title 14 Vol 1 Part 25 - Airworthiness Standards: Transport Category Airplanes*, 2020. URL https://ecfr.federalregister.gov/current/title-14/chapter-I/subchapter-C/part-25.

[15] Boeing, *777-200/300 Airplane Characteristics for Airport Planning*, Boeing Commercial Airplanes, 1998.

[16] Vrancken, P., "Airborne Remote Detection of Turbulence with Forward-Pointing LIDAR," *Aviation Turbulence - Processes, Detection, Prediction*, edited by R. Sharman and T. Lane, Springer, 2016, Chap. 22, pp. 443–464. ISBN: 978-3-319-23629-2.

[17] Herbst, J., and Vrancken, P., "Design of a monolithic Michelson interferometer for fringe imaging in a near-field, UV, direct-detection Doppler wind lidar," *Applied Optics*, Vol. 55, No. 25, 2016, p. 6910. https://doi.org/10.1364/AO.55.006910, URL https://www.osapublishing.org/abstract.cfm?URI=ao-55-25-6910.

[18] Vrancken, P., and Herbst, J., "Development and Test of a Fringe-Imaging Direct-Detection Doppler Wind Lidar for Aeronautics," *EPJ Web of Conferences*, Hefei, People's Republic of China, 2019. URL https://elib.dlr.de/123605/.

[19] Herbst, J., "Development and test of a UV lidar receiver for the measurement of wind velocities aiming at the near-range characterization of wake vortices and gusts in clear air," Dissertation, Ludwig-Maximilians-Universität, Munich, Germany, Apr. 2019.

[20] Vrancken, P., and Herbst, J., "A Novel Direct-Detection Doppler Wind Lidar Based on a Fringe-Imaging Michelson Interferometer as Spectral Analyzer," *2nd European Lidar Conference*, Granada, Spain (virtual), 2020. URL https://elib.dlr.de/cgi/users/home?screen=EPrint%3A%3AView&eprintid=138976.

[21] Rye, B., and Hardesty, R., "Discrete spectral peak estimation in incoherent backscatter heterodyne lidar. I. Spectral accumulation and the Cramer-Rao lower bound," *IEEE Transactions on Geoscience and Remote Sensing*, Vol. 31, No. 1, 1993, pp. 16–27. https://doi.org/10.1109/36.210440.

[22] Bruneau, D., "Mach–Zehnder interferometer as a spectral analyzer for molecular Doppler wind lidar," *Applied Optics*, Vol. 40, No. 3, 2001, pp. 391–399. https://doi.org/10.1364/AO.40.000391, URL https://www.osapublishing.org/ao/abstract.cfm?uri=ao-40-3-391.

[23] Cezard, N., "Etude de faisabilité d'un lidar Rayleigh-Mie pour des mesures à courte portée de la vitesse de l'air, de sa température et de sa densité," thesis, Palaiseau, Ecole polytechnique, Jan. 2008. URL http://www.theses.fr/2008EPXX0022.

[24] McKay, J. A., "Modeling of direct detection Doppler wind lidar I The edge technique," *Applied Optics*, Vol. 37, No. 27, 1998, p. 6480. https://doi.org/10.1364/AO.37.006480, URL https://www.osapublishing.org/abstract.cfm?URI=ao-37-27-6480.

[25] Tucker, S. C., Weimer, C. S., Baidar, S., and Hardesty, R. M., "The Optical Autocovariance Wind Lidar. Part I: OAWL Instrument Development and Demonstration," *Journal of Atmospheric and Oceanic Technology*, Vol. 35, No. 10, 2018, pp. 2079–2097. https://doi.org/10.1175/JTECH-D-18-0024.1, URL http://journals.ametsoc.org/doi/10.1175/JTECH-D-18-0024.1.

[26] Weitkamp, C. (ed.), *Lidar: range-resolved optical remote sensing of the atmosphere*, No. 102 in Springer series in optical sciences, Springer, New York, 2005.

[27] Schmitt, N., Rehm, W., Pistner, T., Zeller, P., Diehl, H., and Navé, P., "The AWIATOR airborne LIDAR turbulence sensor," *Aerospace Science and Technology*, Vol. 11, No. 7-8, 2007, pp. 546–552. https://doi.org/10.1016/j.ast.2007.03.006.

[28] Endemann, M., "ADM-Aeolus: the first spaceborne wind lidar," Goa, India, 2006, p. 64090G. https://doi.org/10.1117/12.697081, URL http://proceedings.spiedigitallibrary.org/proceeding.aspx?doi=10.1117/12.697081.

[29] Tikhonov, A. N., and Arsenin, V. Y., *Solutions of Ill-Posed Problems*, Winston and Sons, Washington, DC, USA, 1977.

[30] Tikhonov, A. N., Goncharsky, A., Stepanov, V. V., and Yagola, A. G., *Numerical Methods for the Solution of Ill-Posed Problems*, Springer-Science+Business Media, B.V., Dordrecht, The Netherlands, 1995. ISBN-13: 978-0-7923-3583-2.

[31] Fezans, N., Joos, H.-D., and Deiler, C., "Gust load alleviation for a long-range aircraft with and without anticipation," *CEAS Aeronautical Journal*, 2019. https://doi.org/10.1007/s13272-019-00362-9.

[32] Fezans, N., "An Unusual Structure for a Feedforward Gust Load Alleviation Controller," *Advances in Aerospace Guidance, Navigation and Control*, edited by B. Dołęga, R. Głębocki, D. Kordos, and M. Żugaj, Springer International Publishing, Cham, 2018, pp. 47–68. https://doi.org/10.1007/978-3-319-65283-2_3, URL http://link.springer.com/10.1007/978-3-319-65283-2_3.

[33] Kubica, F., and Madelaine, B., "Passenger Comfort Improvement by Integrated Control Law Design," Ottawa, Canada, 1999.

[34] Zuo, L., and Nayfeh, S., "Low order continuous-time filters for approximation of the ISO 2631-1 human vibration sensitivity weightings," *Journal of Sound and Vibration*, Vol. 265, No. 2, 2003, pp. 459–465. https://doi.org/10.1016/S0022-460X(02)01567-5, URL https://linkinghub.elsevier.com/retrieve/pii/S0022460X02015675.

[35] Khalil, A., and Fezans, N., "Performance Enhancement of Gust Load Alleviation Systems for Flexible Aircraft using H_∞ Optimal Control with Preview," *AIAA Scitech 2019 Forum*, American Institute of Aeronautics and Astronautics, San Diego, California, 2019. https://doi.org/10.2514/6.2019-0822, URL https://arc.aiaa.org/doi/10.2514/6.2019-0822.

[36] Ly, U.-L., and Chan, Y., "Time-domain computation of aircraft gust covariance matrices," *6th Atmospheric Flight Mechanics Conference*, American Institute of Aeronautics and Astronautics, Danvers,MA,U.S.A., 1980. https://doi.org/10.2514/6.1980-1615, URL https://arc.aiaa.org/doi/10.2514/6.1980-1615.